Inducing Conductive Surface Layer on Nb_2O_5 via Argon-Ion Bombardment: Enhanced Electrochemical Performance for Li-Ion Batteries

Shaoning Zhang,[a] *Jinkwang Hwang*,[a *] *Yuta Sato*,[b] *Kazuhiko Matsumoto*,[a *] *Rika Hagiwara* [a]

a. Graduate School of Energy Science, Kyoto University, Yoshida-honmachi, Sakyo-ku, Kyoto 606-8501, Japan

b. Nanomaterials Research Institute, National Institute of Advanced Industrial Science and Technology (AIST), Central 5, 1-1-1 Higashi, Tsukuba, Ibaraki, 305-8565, Japan

*Corresponding Author

E-mail: k-matsumoto@energy.kyoto-u.ac.jp (K.M.) and hwang.jinkwang.5c@kyoto-u.ac.jp (J.H)

ABSTRACT

Niobium pentoxide (Nb_2O_5) is in the limelight as a negative electrode material for advanced electrical energy storage devices owing to its unique pseudocapacitive behavior. However, its intrinsic poor electronic conductivity restricts its electrochemical performance. In this study, argon-ion bombardment is employed to enhance the interfacial properties of the Nb_2O_5 negative electrode by introducing highly conductive NbO_x ($1 \leq x \leq 2$) species on the electrode surface. Detailed analysis by X-ray photoelectron spectroscopy analyses (XPS) and transition electron microscope (TEM) observation reveals that introducing the surface NbO_x layer which promotes charge transfer at the electrode surface and breaks the limitations of charge transfer resistance in electrochemical measurements. The NbO_x surface architecture fosters improvements in the electrochemical performance of the argon-ion bombarded electrode, exhibiting a higher reversible capacity of 211 mAh g^{-1} than that of pristine electrodes (138 mAh g^{-1}). Electrochemical impedance spectroscopic analysis reveals that introducing the surface NbO_x layer promotes charge transfer at the electrode surface and breaks the limitations of charge transfer resistance. The result provides a pathway to enhance intrinsic shortness of conductivity and to establish surface modification simultaneously via a simple argon-ion bombardment method, thus achieving the improved electrochemical performance of Nb_2O_5.

Keywords: niobium oxides; Ar-ion bombardment; lithium-ion batteries; rate capabilities; electronic conductivity

INTRODUCTION

The surging demand for advanced electrochemical storage devices has shifted development focus into high energy- and power-density electrode materials in efforts to meet modern energy needs.[1-5] Among secondary batteries, niobium pentoxide (Nb_2O_5), specifically its orthorhombic polymorph has gained attention as a high-performance negative electrode material with a high theoretical capacity of 201.7 mAh g^{-1} based on Nb^{5+}/Nb^{4+}, exhibiting superior electrochemical performances emanating from pseudocapacitive Li^+ insertion mechanism(s).[2, 6-10] Even so, the stoichiometric Nb_2O_5 is an insulator with a wide bandgap (between 3.2 and 4.0 eV) which engenders poor electronic conductivity ($\sigma \sim 3\times10^{-6}$ S cm^{-1} at 300 K), thereby improving the poor electronic conductivity is key to achieve a high-rate performance of Nb_2O_5 which eventually facilitate the realization of fast rechargeable energy devices.[11-13] To overcome the drawback, considerable efforts have been devoted to investigating fabrication techniques such as building special morphology, introducing conductive carbon networks, doping foreign elements for adequate utilization, and nanoarchitecture current collector.[14-29] Although materials with the utilization of these methods show certain enhancements, the compatibility with the ongoing manufacturing line remains challenging to meet the requirement of practical utilization of as mentioned methods. A simple experimental design is still highly desirable to circumvent the multistep or complicated synthesis routes.

The modified transition metal oxides, such as the oxides with lower oxidation state, often lead to improved electronic conductivity and electrochemical performance.[30-32] In the niobium oxides, lower oxidation states of Nb-O systems (NbO_x, $1 \leq x \leq 2$) exhibit significantly smaller band gaps and higher electrical conductivities (**Figure 1**). NbO is known to show metallic behavior (10^{-2} to 10^{1} S cm^{-1}).[33-34] This behavior was investigated by calculating its band structure, where the rock salt type structure with low Nb and O occupancies (75%) results in the lowering of Nb 4d

orbital with respect to O 2s and the zero band gap state.[32-34] NbO_2 is a semiconductor with a small band gap of 0.3 eV which is smaller than that of stoichiometric Nb_2O_5 (theoretically indirect band gap of 2.55 eV), showing electronic conductivities (~10^{-4} S cm^{-1}) approximately two orders of magnitude higher than the orthorhombic Nb_2O_5.[35-36] The band gaps of Nb_2O_5 and NbO_2 calculated in a previous paper indicated that the band structure significantly changes from Nb_2O_5 and NbO_2 along with the change in the crystal structure.[33] The different transition modes (G to A for Nb_2O_5 and N to G for NbO_2) and orbital contributions (valence bond maximum state: hybridization of O 2p and Nb 4d orbitals with a little contribution of Nb 4s orbital for Nb_2O_5 and hybridization of O 2p and Nb 4d orbitals for NbO) causes this difference in the band gap.

Argon-ion bombardment (AIB) is widely used for the freshness and removal of the surface of the materials, whereas the concomitant reduction of some metal oxides, such as iron, cobalt, titanium, and niobium by ion-beam bombardment due to preferential sputtering of oxygen has been investigated since the 1970s but remained rarely well-known.[37-39] Previous studies revealed two target processes occur during the AIB: (i) Argon ions and oxygen atoms collide and oxygen atoms subsequently reflect from niobium atoms; (ii) argon ions backscattered from niobium atoms sputter oxygen atoms. These two mechanisms effectively remove oxygen atoms from the surface of Nb_2O_5 especially in a lower energy regime, because deeper penetration of argon ions make these mechanisms less applicable in a higher energy regime. As illustrated in **Figure 1**, it is expected that the introduction of conductive NbO_x species and surface modification could be achieved simultaneously to improve the electrochemical performance via a short-term AIB exposure for several seconds.

In a bid to exploit this strategy, we report a one-step approach for introducing highly conductive NbO_x species on the surface of a Nb_2O_5 electrode through low-energy AIB. Herein,

Nb_2O_5 electrodes treated by AIB for varied durations are characterized and subjected to electrochemical performance tests to determine their feasibility as Li-ion battery negative electrodes. Moreover, the present methodological strategy provides a simple and competitive way to improve low-conductivity of Nb_2O_5 compared to other reduction methods.[40]

EXPERIMENTAL SECTION

Materials and Handling. All the materials were handled under a dry Ar atmosphere in a glove box (H_2O < 1 ppm and O_2 <1 ppm). Nb_2O_5 (Wako Pure Chemical Industries, purity: 99.9%) was used to prepare electrode materials without further purification. The organic electrolyte, 1 M $LiPF_6$-EC/DMC (1:1 v/v; battery grade), was purchased from Kishida Chemical and used without further purification. The Li[FSA]-[C_2C_1im][FSA] ([FSA]$^-$ = bis(fluorosulfonyl)amide and [C_2C_1im]$^+$ = 1-ethyl-3-methylimidazolium) ionic liquid electrolyte was prepared by mixing Li[FSA] and [C_2C_1im][FSA] in 20:80 mol% (1.1 mol dm^{-3}).

Preparation of Electrodes and Cells. A slurry was prepared by mixing the commercial Nb_2O_5, Super C65 (Timcal Ltd.), and Polyamide-imide (PAI) binder in the ratio of 70:20:10 wt% in *N*-methylpyrrolidone (NMP) using a planetary mixer (AR-100, Thinky). The resulting slurry was pasted on Cu foil and was dried under vacuum at 120 °C for 12 h. The electrodes were punched into 10 mm diameter discs. The Argon-ion bombardment (AIB) was carried using a Kaufman-type high etching rate ion gun (JEOL, XP-02300HRIS) at a beam energy of 500 eV and ion current of 8.9 mA. The Argon-ion beam was flashed to the Nb_2O_5 electrode for 15, 30, 60, 90, 120 and 180 s. Each AIB treatment was applied several times of 15 s duration and 15 s rests to avoid overheating. Prepared electrodes have an average mass loading of around 1.2 mg cm^{-2} with a thickness of 50 μm. Coin cells of type-2032 were assembled with the 1 M $LiPF_6$-EC/DMC (1:1 v/v) electrolyte,

the prepared Nb_2O_5 electrode, and Li metal (Sigma-Aldrich Chemistry, 99.95% purity) fixed on stainless steel (SUS316L) plate as a counter electrode.

Material Characterization. The change of oxidation state of Nb_2O_5 after AIB was analyzed by XPS (JOEL, JPS-9030) with Mg*K*α line as the exciting radiation. The morphology of the prepared samples was observed by field emission scanning electron microscopy (FE-SEM) (Hitachi, SU-8020). X-ray diffraction patterns of the samples were recorded in the Bragg-Brentano geometry using a Rigaku SmartLab diffractometer with Ni-filtered Cu-*K*α radiation (40 kV and 30 mA) and a silicon strip high-speed detector (Rigaku D/teX Ultra 250). For the TEM samples preparation, the samples were scratched from the electrodes and put into airtight bottles in a glovebox. 5 mL of super dehydrated NMP was added to the bottles and sonicated for 5 minutes. The Cu grids were immersed in the bottles for 5 sec, and vacuum dried for 24 h at 60 °C. The resulting sample was observed by transmission electron microscopy (TEM, JEOL JEM-2100F) at 60 kV.

Electrochemical Measurements. The electrochemical data were measured by an HJ-SD8 charge-discharge system (Hokuto Denko) and VSP potentiostat (Bio-Logic) at 25 °C. A current density of 200 mA g^{-1} was applied to charge-discharge tests. Discharge rate performance was performed at various discharge current rates from 200 to 40000 mA g^{-1} while the charge current rate was maintained to be 200 mA g^{-1}. Cyclic voltammetry (CV) was performed at a scan rate from 0.5 to 5 mV s^{-1}. Electrochemical impedance spectroscopy (EIS) was conducted in a frequency range from 0.01 Hz to 100 kHz. The half-cell EIS was conducted using the Nb_2O_5 electrode and Li metal counter electrode. The symmetric-cell EIS was conducted using the electrodes after adjusting their voltage to 1.5 V in a half-cell setup.

RESULTS AND DISCUSSION

Characterization of Nb_2O_5 Electrode and AIB Treatment. X-ray photoelectron spectroscopy (XPS) was performed on Nb_2O_5 electrodes exposed to AIB for varied durations (hereafter, Nb_2O_5-AIB*xx* where *xx* denotes the AIB duration in seconds) to ascertain the presence of NbO_x species (**Figure 2a,b)**. The pristine Nb_2O_5 spectra display Nb $3d_{5/2}$ and $3d_{3/2}$ peaks, which are assigned to Nb^V, at the binding energies of 206.3 and 209.6 eV, respectively.[41] The additional peaks at lower binding energy observed in the Nb_2O_5-AIB*xx* spectra ascribed to the Nb^{IV} and Nb^{II} oxidation states.[42-43] The additional peaks at lower binding energy observed in the Nb_2O_5-AIB*xx* spectra ascribed to the Nb^{IV} and Nb^{II} oxidation states with protracted treatment, suggesting progressive Nb_2O_5 reduction resulting from the extending the AIB durations (see **Figure 2b** and **Table S1** for details of deconvoluted peak assignments). To investigate the effect of AIB irradiation on the phase composition of Nb_2O_5 electrodes, all samples are examined by X-ray diffraction (XRD) (**Figure 2c**). XRD patterns reveal that the orthorhombic Nb_2O_5 crystal lattice is preserved irrespective of the AIB duration, indicating the Nb^{IV} and Nb^{II} species exclusively exist on the Nb_2O_5 electrode surface. The FE-SEM images show morphology changes in the surface, seen particle edges becoming rougher and blurred with protracted AIB exposure due to extended oxygen sputtering from the Nb_2O_5 surface (**Figure 2d**).[37, 39] The surface modification by AIB was manifested by TEM observation. The high-resolution (HR)-TEM micrographs and the fast Fourier transform

(FFT) power suggest that AIB treatment reduces the surface (~5 nm) of Nb_2O_5 to NbO_2, showing lattice fringes with d = 0.406 nm corresponding to the diffraction indices of 001 for Nb_2O_5, d = 0.334 and 0.282 nm for 400 and 112 of NbO_2 respectively, d = 0.221 nm indicate 200 of NbO (**Figure 3**). Additional TEM images in **Figure S1** provide more evidence of the existence of a reduced NbO_x layer, showing distinguished phases with different *d*-spacing values in regions A and B, near and away from the surface, respectively. On the one hand, the *d*-spacing value of 0.169 nm is assigned to the diffraction index of 800 for NbO_2 or 211 for NbO observed in the near-surface region (region A), which is in agreement with XPS results of the existence of Nb^{IV} and Nb^{II} species after the AIB treatment. On the other hand, in region B, the *d*-spacing values of 0.578, 0.325, and 0.323 nm correspond to the diffraction indices of 120, 111, and 121 for Nb_2O_5, respectively. The TEM observation confirms the successful introduction of NbO_x species on the surface of the particle of Nb_2O_5 electrode materials through AIB treatment.

Electrochemical Performance of Nb_2O_5-AIB Electrodes. The electrochemical performance of the pristine Nb_2O_5 and Nb_2O_5-AIB electrodes was investigated using Li/Nb_2O_5 cells with 1 M $LiPF_6$-EC/DMC electrolyte at 25 °C. In the 1.0−2.3 V voltage range, lithium insertion occurs into Nb_2O_5, which was proved by the reversible XRD diffraction peaks during (de)lithiation.[10, 44] Figure 4a shows Nb_2O_5-AIB30 attained a considerably higher capacity of 211 mAh g^{-1}, than the pristine Nb_2O_5 (138 mAh g^{-1}) at a current density of 40 mA g^{-1}, which reaches the theoretical capacity of $Nb^{V/IV}$ reaction (211 mAh g^{-1}). For insight into the rate capabilities, current density was varied between 200 and 40000 mA g^{-1} during discharge and fixed at 200 mA g^{-1} during charge (Figure 4b, S2 and Table S2). Here, Nb_2O_5-AIB30 achieves higher rate capabilities than the pristine Nb_2O_5, delivering capacities of 132, 76, and 22 mAh g^{-1} at the discharge rates of 200, 2000, and 10000

mA g^{-1}, respectively. Rate capability tests were also performed under the same charging and discharging current densities, which demonstrated the similar beneficial effect of AIB treatment on rate capabilities (**Figure** S3). However, it is worth noting that although prolonged AIB treatment yielded higher amounts of NbO_x, the rate capability did not improve when the AIB duration was extended to 120 s (**Figure** S2e,f). It is thought that protracted AIB treatment-induced chemical damage on the electrode material, conductive material, and binder (see **Figure** 2d for morphology changes during AIB treatment), results in inferior rate performance, as exhibited by Nb_2O_5-AIB180. The previous studies reported high rate capability with nanostructured or nanosized Nb_2O_5,[25,42,43] which may give the impression that the AIB-treated samples are not competitive to the previous reports. However, it is worth noting that materials with high surface area inevitably face redundant irreversible capacity and low Coulombic efficiency due to electrolyte decomposition and SEI formation.[42,43] It is worth noting that the Nb_2O_5 utilized in the current study is in the bulk state, reaching the theoretical capacity as AIB-treated and improving rate performance as well.

Moreover, the corresponding dQ/dV plots (**Figure 4c**) indicate that voltage polarization was lower in Nb_2O_5-AIB30 than in pristine Nb_2O_5, which was in the agreement with CV results showing higher current value and lower polarization in the AIB30 electrodes (**Figure S4**). These impressive results indicate the beneficial influence of induced NbO_x species on electronic conductivity. Although the direct measurement of electronic conductivity was difficult for the AIB-treated Nb_2O_5, the electrical conductivities of pristine Nb_2O_5 and Nb_2O_5-AIB30 electrodes were evaluated from DC resistances utilizing a two-electrode ion-blocking cell configuration, and the corresponding illustration is shown in **Figure S5**. It was quantitively proved that the electrical conductivity of the entire increases over an order of magnitude, from pristine Nb_2O_5 (2.5×10^{-4} S

cm^{-1}) electrode to Nb_2O_5-AIB30 (1.3×10^{-3} S cm^{-1}) electrode. Additionally, cycle performance tests were conducted at the current density of 200 mA g^{-1} after an aging process entailing 5 cycles at 40 mA g^{-1} followed by 5 cycles at 100 mA g^{-1} (**Figure 4d**, **S6** and **Table S3**). Stable cycling performance is achieved over 300 cycles, wherein the Nb_2O_5-AIB30 delivers discharge capacities 150% higher than the pristine Nb_2O_5. Moreover, the higher capacity retention of 300th vs. 1st cycle is seen in the measurement of and cycling performance for Nb_2O_5-AIB30 electrode than that of the pristine electrode (80% for Nb_2O_5-AIB30 and 66% for pristine Nb_2O_5, **Table S3**). The FE-SEM images (Figure S7) show differences in the surface condition between pristine and Nb_2O_5-AIB30 electrodes after cycle tests. The edges of Nb_2O_5-AIB30 particle sustain clearly after cycling test which may indicate a higher conductive layer induced by AIB is a more favorable interfacial environment for the cycling tests. Indicating a higher conductive layer of AIB-induced NbO_x species may provide a more favorable interfacial environment for cycling tests. These results, therefore, establish the beneficial influence of AIB-induced NbO_x species on the electrochemical performance of AIB30 electrodes, and NbO_x species is maintained after the cycling test (see **Figure S8** for XPS measurement after 300 cycles). Cycling performance tests were also conducted under a high current density of 2000 mA g^{-1} (ionic liquid electrolyte was used to maintain a stable performance Li metal counter electrode),[45] which demonstrated a similar beneficial effect of AIB treatment on discharge capacities (**Figure S9**).

Electrochemical Impedance Spectroscopy Analysis. To assess the electrode interfacial behavior, electrochemical impedance spectroscopy (EIS) was performed on half- and symmetric-cell configurations at 1.5 V. The symmetric cell EIS is a simple and powerful method which comprises two identical electrodes to eliminate the influence of the counter electrode. Typically, two identical half-cells are prepared for electrochemical measurements, and the two targeting electrodes are used

for the symmetric cell.[46-49] According to the Nyquist plots of the pristine Nb_2O_5 and Nb_2O_5-AIB30 electrodes obtained in half and symmetric cell EIS (**Figure 5a,b**, **S10**), a substantial decrease was observed in the semi-circles corresponding to the resistance upon AIB treatment, evincing that AIB introduced NbO_x promotes charge transfer at the electrode surface (see **Figure S11** and Table S4 for EIS fitting results and utilized equivalent circuit). This is an explicit explanation for rate capability improvement and decrease of polarization after AIB treatment on Nb_2O_5 electrode. To gain a more quantitative measure for the kinetics of electrochemical reaction for Nb_2O_5-AIB electrodes, the EIS was conducted in symmetric cell configuration at various temperatures from 10 to 25 °C, and the activation energies of R_{ct} were calculated in the following equation.[50-51]

$$\ln\left(\frac{1}{R}\right) = -\left(\frac{E_a}{R_g}\right)\left(\frac{1}{T}\right) + \ln(A)$$

Here, A is the frequency factor, R is the resistance of charge transfer, R_g is the gas constant and T is the absolute temperature. E_a is activation energy and calculated by the slope of the linear fitted line shown in **Figure 5c**. The E_a value for R^{-1} is 86.9 kJ mol^{-1} at a duration of the pristine Nb_2O_5 and decreased to 62.4 kJ mol^{-1} for the Nb_2O_5-AIB30. The corresponding Arrhenius plot manifested lower activation energy in Nb_2O_5-AIB30 (compared to the pristine electrode) for the reciprocal charge transfer resistance, contributing to the obtained enhanced electrochemical.

CONCLUSIONS

This study proposes an expedient one-step strategy for ameliorating the limited electronic conductivity of the Nb_2O_5 negative electrode using low-energy AIB. Electrodes exposed to AIB exhibit significantly enhanced electrochemical performance attributed to the presence of

electrically conductive NbO_x species on the electrode surface. Therefore, this report demonstrates surface modification as a straightforward avenue for broadening the utility of low electronic conductivity materials in advanced energy storage systems. Although the batch treatment procedure for AIB limits the treatable area, the short treatment time is its big advantage. The AIB methodology is expected to be applied in the practical process flow of electrode materials by developing a suitable technology on Argon-ion beam exposure in the near future. Even so, information on the atomistic mechanisms behind the interfacial properties remains limited, highlighting the need for further experimental and theoretical inquests into AIB.

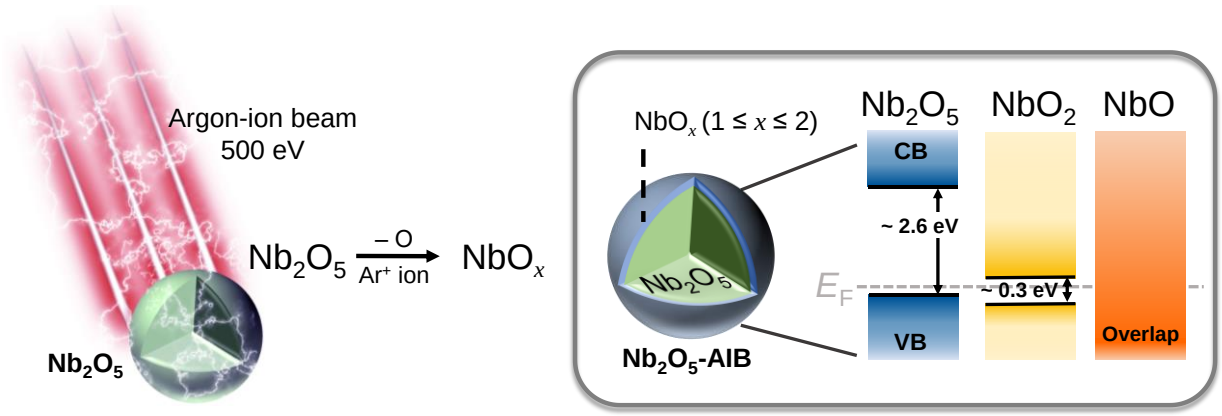

Figure 1. Schematic illustration of niobium oxides electronic band structure including Nb_2O_5, NbO_2 and NbO, and introducing NbO_x conductive layer on Nb_2O_5 electrode by AIB treatment.

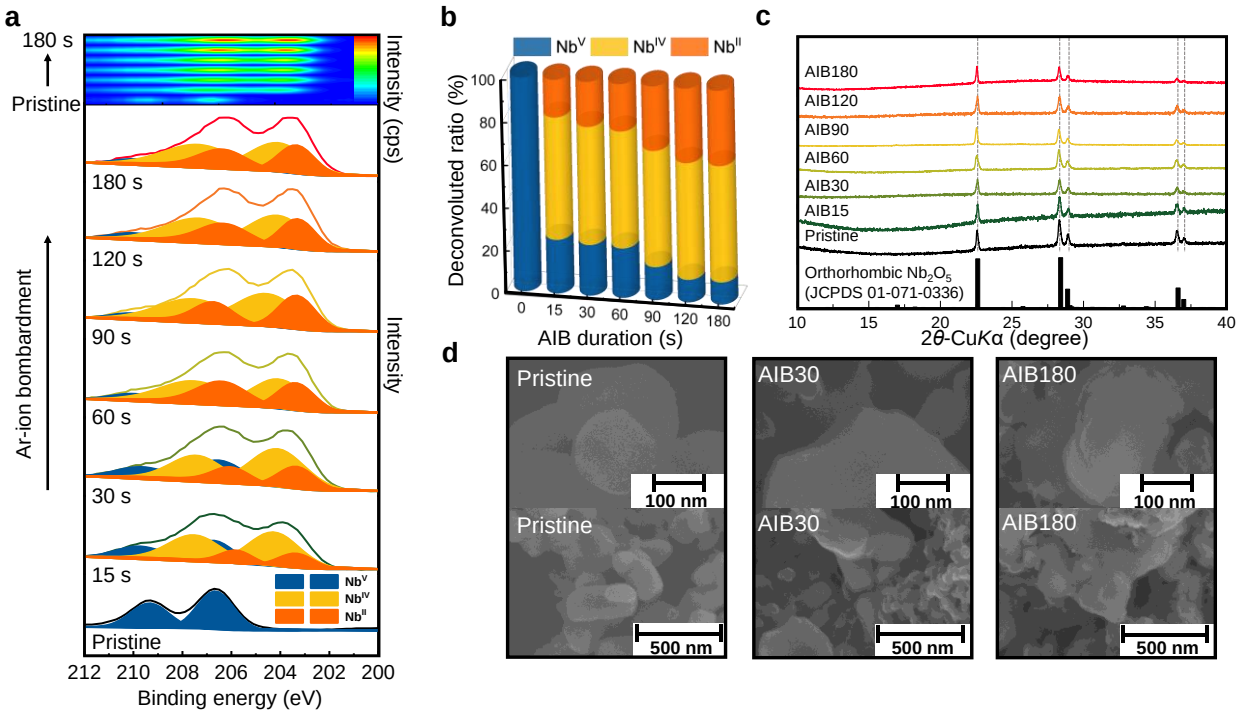

Figure 2. Characterization of pristine Nb_2O_5 and Nb_2O_5-AIB*xx* (*xx* =15, 30, 60, 90, 120, and 180 seconds) electrodes. (a) XPS spectra of the pristine Nb_2O_5 and Nb_2O_5-AIB*xx* electrodes. The Nb 3d peaks show the changes in Nb valence states with increasing AIB duration. (b) Ratio of Nb oxidation states on the surface of pristine Nb_2O_5 and Nb_2O_5-AIB*xx* electrodes. See Table S1 for peak assignment and deconvoluted ratios of each Nb_2O_5-AIB*xx* electrode sample. (c) XRD patterns of the pristine Nb_2O_5 and Nb_2O_5-AIB*xx* electrodes. Reference patterns of the orthorhombic Nb_2O_5 are reproduced from previous data (JCPDS 01-071-0336).[52] (d) FE-SEM images of pristine Nb_2O_5, Nb_2O_5-AIB30, and Nb_2O_5-AIB180.

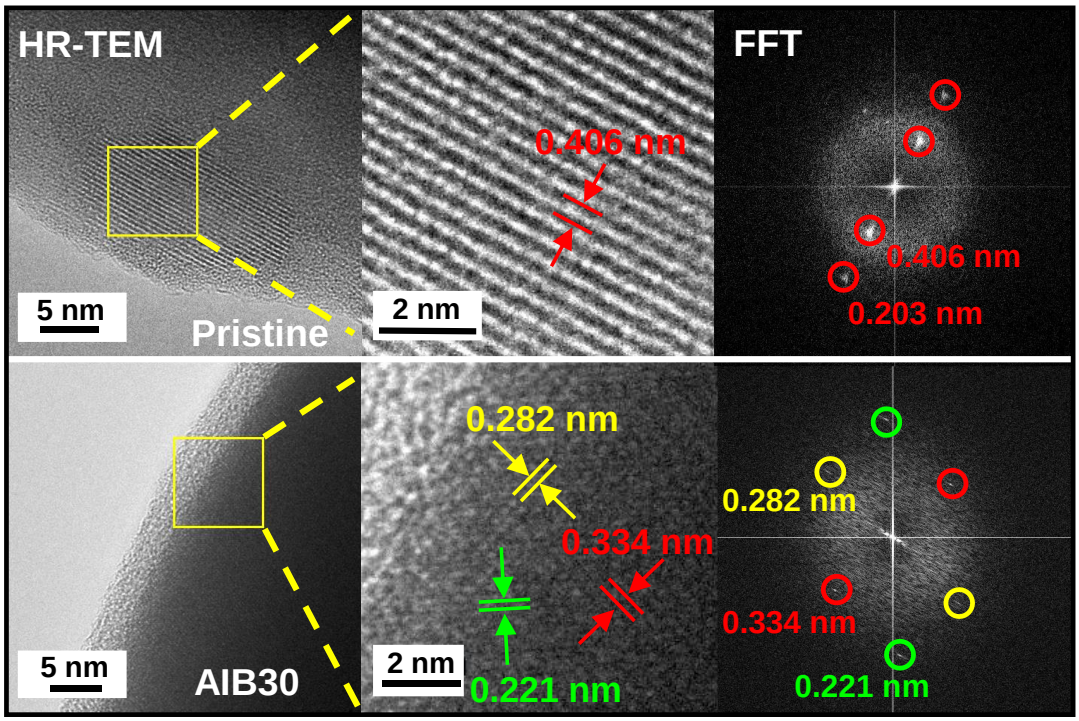

Figure 3. HR-TEM and corresponding FFT of the pristine Nb_2O_5 and Nb_2O_5-AIB30 electrodes.

See **Figure S1** for additional TEM images for Nb_2O_5-AIB30 electrodes.

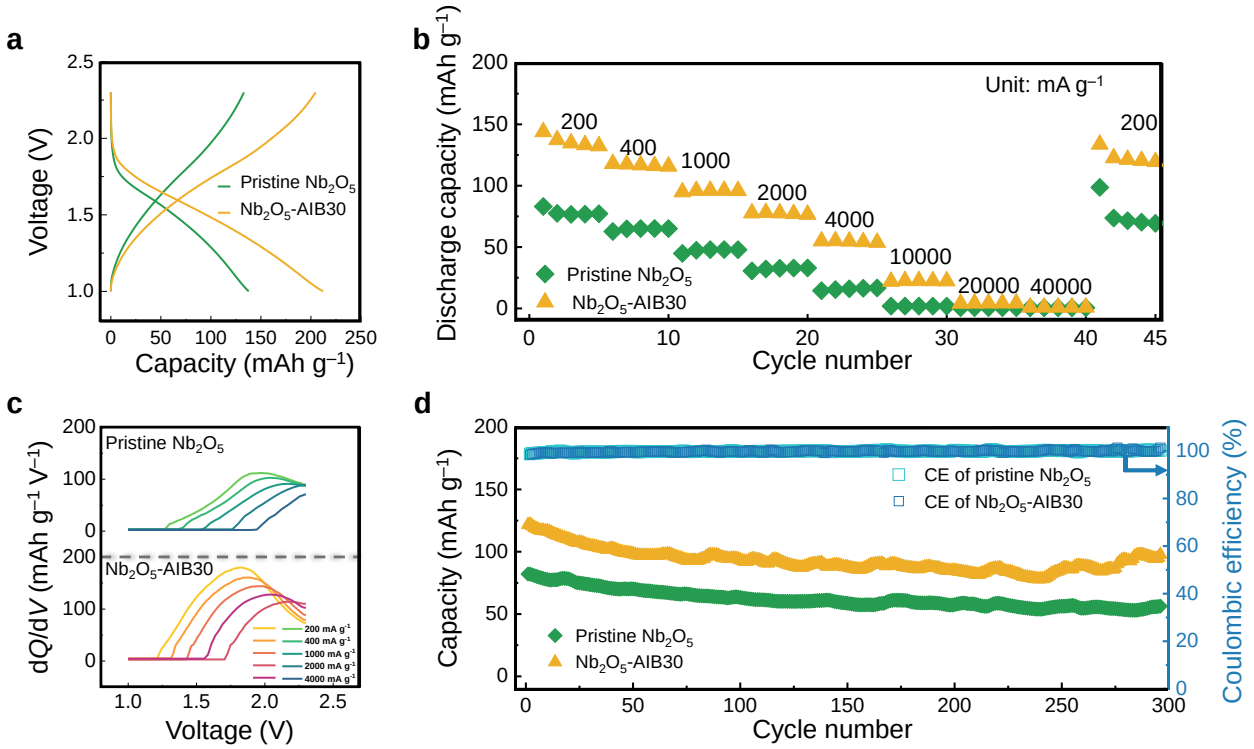

Figure 4. Electrochemical performance of pristine Nb_2O_5 and Nb_2O_5-AIB30 electrodes. Electrolyte: 1M $LiPF_6$-ECDMC. (a) Charge-discharge curves in the 1.0–2.3 V cutoff voltage range at the current density of 40 mA g^{-1}. (b) Comparative rate capabilities. Current density during charge: 200 mA g^{-1}. Current density during discharge: 200–40000 mA g^{-1} (see **Figure S2** for the respective discharge profiles and **Table S2** for capacity and capacity retention). (c) Corresponding d*Q*/d*V* plots for the rate capability tests in (b). (d) Comparative cycle performance. Current densities for both charge and discharge: 200 mA g^{-1} and cutoff voltage range: 1.0–2.3 V (see **Figure S6** for the corresponding charge-discharge curves and **Table S3** for details of capacity and capacity retention during cycle performance).

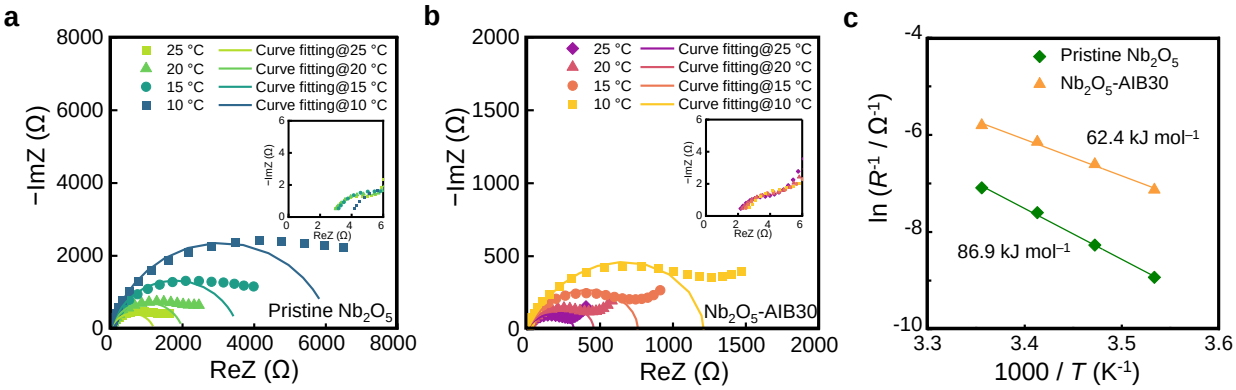

Figure 5. Comparative (a, b) Nyquist plots of the pristine Nb_2O_5 and Nb_2O_5-AIB30 symmetric cells at state of charge of 1.5 V at various temperatures. The high-frequency region of (a,b) are shown in the inset, respectively. Electrolyte: 1M $LiPF_6$-ECDMC. (c) Corresponding Arrhenius plots of symmetric cells. Frequency range: 0.01 Hz – 100 kHz. AC amplitude: 10 mV. Characteristic frequencies for the semicircle are: 1 – 0.5 Hz. See **Figure S11** and **Table S4** for utilized equivalent circuit to fit the Nyquist plots and fitting results.

ASSOCIATED CONTENT

Supporting Information.

The Supporting Information is available free of charge at DOI: xx.

Additional TEM micro-graph, additional electrochemical properties with additional discussion, and peak assignment for XPS data, fitting result for the Nyquist plots. (PDF)

AUTHOR INFORMATION

Corresponding Author

Jinkwang *Phone: +81 75 753 5827. Fax: +81 75 753 5906.

E-mail: hwang.jinkwang.5c@kyoto-u.ac.jp and k-matsumoto@energy.kyoto-u.ac.jp

ORCID

Shaoning. Zhang: 0000-0003-1727-5863

Jinkwang Hwang: 0000-0003-4800-3158

Yuta Sato: 0000-0002-4231-6287

Kazuhiko Matsumoto: 0000-0002-0770-9210

Rika Hagiwara: 0000-0002-7234-3980

Notes

The authors declare no competing financial interest.

ACKNOWLEDGMENT

This study was supported by the Japan Society for the Promotion of Science (JSPS, KAKENHI Grant Number 19H02811).

REFERENCES

(1) Duffner, F.; Kronemeyer, N.; Tübke, J.; Leker, J.; Winter, M.; Schmuch, R. Post-lithium-ion battery cell production and its compatibility with lithium-ion cell production infrastructure. *Nat. Energy* **2021,** *6*, 123-134.

(2) Weiss, M.; Ruess, R.; Kasnatscheew, J.; Levartovsky, Y.; Levy, N. R.; Minnmann, P.; Stolz, L.; Waldmann, T.; Wohlfahrt-Mehrens, M.; Aurbach, D.; Winter, M.; Ein-Eli, Y.; Janek, J. Fast Charging of Lithium-Ion Batteries: A Review of Materials Aspects. *Adv. Energy Mater.* **2021,** *11*, 2101126.

(3) Wu, Y.; Wang, W.; Ming, J.; Li, M.; Xie, L.; He, X.; Wang, J.; Liang, S.; Wu, Y. An Exploration of New Energy Storage System: High Energy Density, High Safety, and Fast Charging Lithium Ion Battery. *Adv. Funct. Mater.* **2019,** *29*, 1805978.

(4) Huang, H.; Niederberger, M. Towards fast-charging technologies in Li^+/Na^+ storage: from the perspectives of pseudocapacitive materials and non-aqueous hybrid capacitors. *Nanoscale* **2019,** *11*, 19225-19240.

(5) Xia, R.; Overa, S.; Jiao, F. Emerging Electrochemical Processes to Decarbonize the Chemical Industry. *JACS Au* **2022,** *2*, 1054-1070.

(6) Chen, D.; Wang, J.-H.; Chou, T.-F.; Zhao, B.; El-Sayed, M. A.; Liu, M. Unraveling the Nature of Anomalously Fast Energy Storage in T-Nb_2O_5. *J. Am. Chem. Soc.* **2017,** *139*, 7071-7081.

(7) Griffith, K. J.; Forse, A. C.; Griffin, J. M.; Grey, C. P. High-Rate Intercalation without Nanostructuring in Metastable Nb_2O_5 Bronze Phases. *J. Am. Chem. Soc.* **2016,** *138*, 8888-8899.

(8) Meng, J.; He, Q.; Xu, L.; Zhang, X.; Liu, F.; Wang, X.; Li, Q.; Xu, X.; Zhang, G.; Niu, C.; Xiao, Z.; Liu, Z.; Zhu, Z.; Zhao, Y.; Mai, L. Identification of Phase Control of Carbon-Confined

Nb_2O_5 Nanoparticles toward High-Performance Lithium Storage. *Adv. Energy Mater.* **2019,** *9*, 1802695.

(9) Cao, D.; Yao, Z.; Liu, J.; Zhang, J.; Li, C. H-Nb_2O_5 wired by tetragonal tungsten bronze related domains as high-rate anode for Li-ion batteries. *Energy Storage Mater.* **2018,** *11*, 152-160.

(10) Zhang, S.; Hwang, J.; Matsumoto, K.; Hagiwara, R. In Situ Orthorhombic to Amorphous Phase Transition of Nb_2O_5 and Its Temperature Effect on Pseudocapacitive Behavior. *ACS Appl. Mater. Interfaces* **2022,** *14*, 19426-19436.

(11) Fichtner, M.; Edström, K.; Ayerbe, E.; Berecibar, M.; Bhowmik, A.; Castelli, I. E.; Clark, S.; Dominko, R.; Erakca, M.; Franco, A. A.; Grimaud, A.; Horstmann, B.; Latz, A.; Lorrmann, H.; Meeus, M.; Narayan, R.; Pammer, F.; Ruhland, J.; Stein, H.; Vegge, T.; Weil, M. Rechargeable Batteries of the Future—The State of the Art from a BATTERY 2030+ Perspective. *Adv. Energy Mater.* **2021,** 2102904.

(12) Zeng, Y.; Chalise, D.; Lubner, S. D.; Kaur, S.; Prasher, R. S. A review of thermal physics and management inside lithium-ion batteries for high energy density and fast charging. *Energy Storage Mater.* **2021,** *41*, 264-288.

(13) Liu, Y.; Zhu, Y.; Cui, Y. Challenges and opportunities towards fast-charging battery materials. *Nat. Energy* **2019,** *4*, 540-550.

(14) Li, T.; Nam, G.; Liu, K.; Wang, J.-H.; Zhao, B.; Ding, Y.; Soule, L.; Avdeev, M.; Luo, Z.; Zhang, W.; Yuan, T.; Jing, P.; Kim, M. G.; Song, Y.; Liu, M. A niobium oxide with a shear structure and planar defects for high-power lithium ion batteries. *Energy Environ. Sci.* **2022,** *15*, 254-264.

(15) Budak, Ö.; Geißler, M.; Becker, D.; Kruth, A.; Quade, A.; Haberkorn, R.; Kickelbick, G.; Etzold, B. J. M.; Presser, V. Carbide-Derived Niobium Pentoxide with Enhanced Charge Storage

Capacity for Use as a Lithium-Ion Battery Electrode. *ACS Appl. Energy Mater.* **2020,** *3*, 4275-4285.

(16) Shen, F.; Sun, Z.; Zhao, L.; Xia, Y.; Shao, Y.; Cai, J.; Li, S.; Lu, C.; Tong, X.; Zhao, Y.; Sun, J.; Shao, Y. Triggering the phase transition and capacity enhancement of Nb_2O_5 for fast-charging lithium-ion storage. *J. Mater. Chem. A* **2021,** *9*, 14534-14544.

(17) Yan, X.; Li, T.; Xiong, Y.; Ge, X. Synchronized ion and electron transfer in a blue T-Nb_2O_{5-x} with solid-solution-like process for fast and high volumetric charge storage. *Energy Storage Mater.* **2021,** *36*, 213-221.

(18) Xia, R.; Zhao, K.; Kuo, L.-Y.; Zhang, L.; Cunha, D. M.; Wang, Y.; Huang, S.; Zheng, J.; Boukamp, B.; Kaghazchi, P.; Sun, C.; ten Elshof, J. E.; Huijben, M. Nickel Niobate Anodes for High Rate Lithium-Ion Batteries. *Adv. Energy Mater.* **2022,** *12*, 2102972.

(19) Sun, Y.-G.; Piao, J.-Y.; Hu, L.-L.; Bin, D.-S.; Lin, X.-J.; Duan, S.-Y.; Cao, A.-M.; Wan, L.-J. Controlling the Reaction of Nanoparticles for Hollow Metal Oxide Nanostructures. *J. Am. Chem. Soc.* **2018,** *140*, 9070-9073.

(20) Lou, S.; Cheng, X.; Wang, L.; Gao, J.; Li, Q.; Ma, Y.; Gao, Y.; Zuo, P.; Du, C.; Yin, G. High-rate capability of three-dimensionally ordered macroporous T-Nb_2O_5 through Li+ intercalation pseudocapacitance. *J. Power Sources* **2017,** *361*, 80-86.

(21) Tang, Y.; Yang, L.; Zhu, Y.; Zhang, F.; Zhang, H. Fabrication of a highly stable Nb_2O_5@C/CNTs based anolyte for lithium slurry flow batteries. *J. Mater. Chem. A* **2022,** *10*, 5620-5630.

(22) Song, M. Y.; Kim, N. R.; Yoon, H. J.; Cho, S. Y.; Jin, H.-J.; Yun, Y. S. Long-Lasting Nb_2O_5-Based Nanocomposite Materials for Li-Ion Storage. *ACS Appl. Mater. Interfaces* **2017,** *9*, 2267-2274.

(23) Song, H.; Fu, J.; Ding, K.; Huang, C.; Wu, K.; Zhang, X.; Gao, B.; Huo, K.; Peng, X.; Chu, P. K. Flexible Nb_2O_5 nanowires/graphene film electrode for high-performance hybrid Li-ion supercapacitors. *J. Power Sources* **2016,** *328*, 599-606.

(24) Cheong, J. Y.; Youn, D. Y.; Kim, C.; Jung, J.-W.; Ogata, A. F.; Bae, J. G.; Kim, I.-D. Ag-coated one-dimensional orthorhombic Nb_2O_5 fibers as high performance electrodes for lithium storage. *Electrochim. Acta* **2018,** *269*, 388-396.

(25) Zhao, Y.; Ding, C.; Hao, Y.; Zhai, X.; Wang, C.; Li, Y.; Li, J.; Jin, H. Neat Design for the Structure of Electrode To Optimize the Lithium-Ion Battery Performance. *ACS Appl. Mater. Interfaces* **2018,** *10*, 27106-27115.

(26) Jiang, Y.; Guo, S.; Li, Y.; Hu, X. Rapid microwave synthesis of carbon-bridged Nb2O5 mesocrystals for high-energy and high-power sodium-ion capacitors. *J. Mater. Chem. A* **2022,** *10*, 11470-11476.

(27) Song, Z.; Li, H.; Liu, W.; Zhang, H.; Yan, J.; Tang, Y.; Huang, J.; Zhang, H.; Li, X. Ultrafast and Stable Li-(De)intercalation in a Large Single Crystal H-Nb_2O_5 Anode via Optimizing the Homogeneity of Electron and Ion Transport. *Adv. Mater.* **2020,** *32*, 2001001.

(28) Zheng, Y.; Yao, Z.; Shadike, Z.; Lei, M.; Liu, J.; Li, C. Defect-Concentration-Mediated T-Nb_2O_5 Anodes for Durable and Fast-Charging Li-Ion Batteries. *Adv. Funct. Mater.* **2022,** *32*, 2107060.

(29) Liu, L.; Zhao, H.; Lei, Y. Review on Nanoarchitectured Current Collectors for Pseudocapacitors. *Small Methods* **2019,** *3*, 1800341.

(30) Hao, J.; Zhang, J.; Xia, G.; Liu, Y.; Zheng, Y.; Zhang, W.; Tang, Y.; Pang, W. K.; Guo, Z. Heterostructure Manipulation via in Situ Localized Phase Transformation for High-Rate and Highly Durable Lithium Ion Storage. *ACS Nano* **2018,** *12*, 10430-10438.

(31) Zeng, Y.; Lai, Z.; Han, Y.; Zhang, H.; Xie, S.; Lu, X. Oxygen-Vacancy and Surface Modulation of Ultrathin Nickel Cobaltite Nanosheets as a High-Energy Cathode for Advanced Zn-Ion Batteries. *Adv. Mater.* **2018,** *30*, 1802396.

(32) Kim, H.-S.; Cook, J. B.; Lin, H.; Ko, Jesse S.; Tolbert, Sarah H.; Ozolins, V.; Dunn, B. Oxygen vacancies enhance pseudocapacitive charge storage properties of MoO_{3-x}. *Nat. Mater.* **2017,** *16*, 454-460.

(33) Roberson, J. A.; Rapp, R. A. Electrical properties of NbO and NbO_2. *J. Phys. Chem. Solids* **1969,** *30*, 1119-1124.

(34) Adler, D. Electrical and optical properties of transition-metal oxides. *Radiation Effects* **1970,** *4*, 123-131.

(35) Hulm, J. K.; Jones, C. K.; Hein, R. A.; Gibson, J. W. Superconductivity in the TiO and NbO systems. *J. Low Temp. Phys.* **1972,** *7*, 291-307.

(36) Weibin, Z.; Weidong, W.; Xueming, W.; Xinlu, C.; Dawei, Y.; Changle, S.; Liping, P.; Yuying, W.; Li, B. The investigation of NbO_2 and Nb_2O_5 electronic structure by XPS, UPS and first principles methods. *Surf. Interface Anal.* **2013,** *45*, 1206-1210.

(37) Choudhury, T.; Saied, S. O.; Sullivan, J. L.; Abbot, A. M. Reduction of oxides of iron, cobalt, titanium and niobium by low-energy ion bombardment. *J. Phys. D Appl. Phys.* **1989,** *22*, 1185-1195.

(38) Murti, D. K.; Kelly, R. Studies on Bombardment-Enhanced Conductivity. IV. *Surf. Sci.* **1975,** *47*, 282-293.

(39) Karulkar, P. C. Effects of sputtering on the surface composition of niobium oxides. *J. Vac. Sci. Technol.* **1981,** *18*, 169-174.

(40) Zhang, J.; He, H.; Tang, Y.; Ji, X.; Wang, H. Advanced Materials Prepared via Metallic Reduction Reactions for Electrochemical Energy Storage. *Small Methods* **2020,** *4*, 2000613.

(41) McGuire, G. E.; Schweitzer, G. K.; Carlson, T. A. Study of Core Electron Binding Energies in Some Group IIIa, Vb, and VIb Compounds. *Inorg. Chem.* **1973,** *12*, 2450-2453.

(42) Jung, K.; Kim, Y.; Park, Y. S.; Jung, W.; Choi, J.; Park, B.; Kim, H.; Kim, W.; Hong, J.; Im, H. Unipolar Resistive Switching in Insulating Niobium Oxide Film and Probing Electroforming Induced Metallic Components. *J. Appl. Phys.* **2011,** *109*.

(43) Bahl, M. K. ESCA Studies of Some Niobium Compounds. *J. Phys. Chem. Solids* **1975,** *36*, 485-491.

(44) Come, J.; Augustyn, V.; Kim, J. W.; Rozier, P.; Taberna, P.-L.; Gogotsi, P.; Long, J. W.; Dunn, B.; Simon, P. Electrochemical Kinetics of Nanostructured Nb_2O_5 Electrodes. *J. Electrochem. Soc.* **2014,** *161*, A718.

(45) Hwang, J.; Okada, H.; Haraguchi, R.; Tawa, S.; Matsumoto, K.; Hagiwara, R. Ionic liquid electrolyte for room to intermediate temperature operating Li metal batteries: Dendrite suppression and improved performance. *J. Power Sources* **2020,** *453*, 227911.

(46) Hwang, J.; Matsumoto, K.; Hagiwara, R. Symmetric Cell Electrochemical Impedance Spectroscopy of $Na_2FeP_2O_7$ Positive Electrode Material in Ionic Liquid Electrolytes. *J. Phys. Chem. C* **2018,** *122*, 26857-26864.

(47) Gaberšček, M. Understanding Li-based battery materials via electrochemical impedance spectroscopy. *Nat. Commun.* **2021,** *12*, 6513.

(48) Zhang, Y.; Tang, Q.; Zhang, Y.; Wang, J.; Stimming, U.; Lee, A. A. Identifying degradation patterns of lithium ion batteries from impedance spectroscopy using machine learning. *Nat. Commun.* **2020,** *11*, 1706.

(49) Ogihara, N.; Kawauchi, S.; Okuda, C.; Itou, Y.; Takeuchi, Y.; Ukyo, Y. Theoretical and Experimental Analysis of Porous Electrodes for Lithium-Ion Batteries by Electrochemical Impedance Spectroscopy Using a Symmetric Cell. *J. Electrochem. Soc.* **2012,** *159*, A1034-A1039.

(50) Sagane, F.; Abe, T.; Iriyama, Y.; Ogumi, Z. Li^+ and Na^+ transfer through interfaces between inorganic solid electrolytes and polymer or liquid electrolytes. *J. Power Sources* **2005,** *146*, 749-752.

(51) Abe, T.; Sagane, F.; Ohtsuka, M.; Iriyama, Y.; Ogumi, Z. Lithium-Ion Transfer at the Interface Between Lithium-Ion Conductive Ceramic Electrolyte and Liquid Electrolyte-A Key to Enhancing the Rate Capability of Lithium-Ion Batteries. *J. Electrochem. Soc.* **2005,** *152*, A2151.

(52) Kato, K.; Tamura, S. Die Kristallstruktur von *T*-Nb_2O_5. *Acta Cryst. B* **1975,** *31*, 673-677.